AGU PUBLICATIONS

JGR

Journal of Geophysical Research: Space Physics

RESEARCH ARTICLE

10.1002/2013JA019657

Special Section:
Fundamental Properties and Processes of Magnetotails

Key Points:
- Tailward moving Bz jump is followed by earthward moving dipolarization front
- Initial substorm signatures associated with the Bz jump propagate tailward
- The tailward Bz jump facilitates strong substorm associated with the later DF

Correspondence to:
K.-J. Hwang,
Kyoung-Joo.Hwang@nasa.gov

Citation:
Hwang, K.-J., M. L. Goldstein, T. E. Moore, B. M. Walsh, D. G. Baishev, A. V. Moiseyev, B. M. Shevtsov, and K. Yumoto (2014), A tailward moving current sheet normal magnetic field front followed by an earthward moving dipolarization front, *J. Geophys. Res. Space Physics*, *119*, 5316–5327, doi:10.1002/2013JA019657.

Received 25 NOV 2013
Accepted 2 JUN 2014
Accepted article online 6 JUN 2014
Published online 1 JUL 2014

A tailward moving current sheet normal magnetic field front followed by an earthward moving dipolarization front

K.-J. Hwang[1,2], M. L. Goldstein[1], T. E. Moore[1], B. M. Walsh[3], D. G. Baishev[4], A. V. Moiseyev[4], B. M. Shevtsov[5], and K. Yumoto[6,7]

[1]NASA Goddard Space Flight Center, Greenbelt, Maryland, USA, [2]Goddard Planetary Heliophysics Institute, University of Maryland, Baltimore County, Baltimore, Maryland, USA, [3]Space Sciences Laboratory, University of California, Berkeley, California, USA, [4]Yu. G. Shafer Institute of Cosmophysical Research and Aeronomy, Siberian Branch of the Russian Academy of Sciences, Yakutsk, Russia, [5]Institute of Cosmophysical Researches and Radio Wave Propagation, Far East Branch of Russian Academy of Sciences, Paratunka, Russia, [6]International Center for Space Weather Science and Education, Kyushu University, Fukuoka, Japan, [7]Department of Earth and Planetary Sciences, Kyushu University, Fukuoka, Japan

Abstract A case study is presented using measurements from the Cluster spacecraft and ground-based magnetometers that show a substorm onset propagating from the inner to outer plasma sheet. On 3 October 2005, Cluster, traversing an ion-scale current sheet at the near-Earth plasma sheet, detected a sudden enhancement of B_z, which was immediately followed by a series of flux rope structures. Both the local B_z enhancement and flux ropes propagated tailward. Approximately 5 min later, another B_z enhancement, followed by a large density decrease, was observed to rapidly propagate earthward. Between the two B_z enhancements, a significant removal of magnetic flux occurred, possibly resulting from the tailward moving B_z enhancement and flux ropes. In our scenario, this flux removal caused the magnetotail to be globally stretched so that the thinnest sheet formed tailward of Cluster. The thinned current sheet facilitated magnetic reconnection that quickly evolved from plasma sheet to lobe and generated the later earthward moving dipolarization front (DF) followed by a reduction in density and entropy. Ground magnetograms located near the meridian of Cluster's magnetic foot points show two-step bay enhancements. The positive bay associated with the first B_z enhancement indicates that the substorm onset signatures propagated from the inner to the outer plasma sheet, consistent with the Cluster observation. The more intense bay features associated with the later DF are consistent with the earthward motion of the front. The event suggests that current disruption signatures that originated in the near-Earth current sheet propagated tailward, triggering or facilitating midtail reconnection, thereby preconditioning the magnetosphere for a later strong substorm enhancement.

1. Introduction

Dipolarization fronts (DFs) are a phenomenon commonly detected near the equatorial plane of the Earth's tail plasma sheet. They are characterized by sharp increases in the magnetic field component normal to the equatorial plane of the magnetosphere, often associated with intense gradients of B_z in geocentric solar magnetospheric (GSM) or geocentric solar ecliptic (GSE) coordinates. Spacecraft typically sees an increase of magnetic pressure and decrease of plasma pressure across the front. Such plasma and magnetic field variations across DFs indicate that they carry an entropy-depleted flux tube, or localized "plasma bubbles" behind them [*Hwang et al.*, 2011; *Sergeev et al.*, 2012]. Numerous DF observations at the near-Earth plasma sheet by the Cluster [e.g., *Nakamura et al.*, 2002; *Hwang et al.*, 2011; *Fu et al.*, 2011, 2012; *Schmid et al.*, 2012; *Hwang et al.*, 2014] and Time History of Events and Macroscale Interactions during Substorms (THEMIS) [e.g., *Runov et al.*, 2009; *Sergeev et al.*, 2009; *Zhou et al.*, 2010; *Deng et al.*, 2010; *Dubyagin et al.*, 2010; *Ashour-Abdalla et al.*, 2011] spacecraft have shown that DFs predominantly propagate earthward along the radial direction and are often embedded within fast earthward flows, i.e., bursty bulk flows [*Angelopoulos et al.*, 1992, 1999].

DFs have drawn wide attention because they significantly affect the acceleration and transport of plasmas [e.g., *Sergeev et al.*, 2009; *Zhou et al.*, 2009; *Deng et al.*, 2010; *Hwang et al.*, 2011; *Fu et al.*, 2011; *Ashour-Abdalla et al.*, 2011; *Birn et al.*, 2013]. The observed energization is attributed to betatron and/or (first-order) Fermi acceleration associated with the local magnetic pileup signature of DFs and the large-scale reconfiguration

(shortening) of the magnetic fields caused by radial convection of DFs [*Birn et al.*, 2003; *Ashour-Abdalla et al.*, 2011; *Fu et al.*, 2011] and to other nonadiabatic processes, including wave-particle interactions [*Deng et al.*, 2010; *Hwang et al.*, 2011, 2014]. DFs are also thought to play a significant role in populating the inner magnetosphere by transporting plasmas from the midtail (15–30 R_E) to the near-Earth (10–15 R_E) plasma sheet and, in some cases, into the inner magnetosphere [*Delcourt et al.*, 1990; *Delcourt*, 2002; *Jones et al.*, 2006; *Runov et al.*, 2009; *Ashour-Abdalla et al.*, 2011]. *Nosé et al.* [2010] presented multiple scenarios to explain transport of O^+ ions from the ionosphere to the ring current and how dipolarization in the magnetotail can contribute to the transport or the significant increase in O^+ fluxes in the ring current during magnetic storms. Moreover, DFs have been implicated in nonadiabatic particle acceleration that might explain the mass-dependent variation of inner-magnetospheric ring current ions (in particular, the observed significant enhancement of energetic O^+ fluxes) during geomagnetic storm time [*Delcourt*, 2002; *Ohtani et al.*, 2005; *Fok et al.*, 2006; *Keika et al.*, 2010].

DFs may arise during global magnetic dipolarization and are often associated with substorm, but the occurrence of DFs does not necessarily imply a substorm dipolarization. However, most DF observations are linked to ionospheric responses and/or auroral signatures at any activity level [*Keika et al.*, 2010; *Nakamura et al.*, 2011; *Hwang et al.*, 2011; *Zhou et al.*, 2012; *Ge et al.*, 2012], which indicates that DFs that commonly form in azimuthally narrow channels cause disturbances in the magnetic field at ionospheric heights that are coupled to the magnetosphere and/or generate field-aligned currents [*Hwang et al.*, 2011]. DFs also appear to contribute to particle precipitation into the ionosphere that produces auroral signatures [*Ge et al.*, 2012; *Zhou et al.*, 2012].

Dipolarization of tailward magnetic topology, which is often accompanied by observation of a DF, has been associated with a decrease of the cross-tail current in the near-Earth region that might be caused by, e.g., a cross-tail current instability [*Lui et al.*, 1991]. *Lui* [1991] presented the synthesis model of substorm development that includes current disruptions leading to convection surges and tailward propagating rarefaction waves and the formation of magnetic reconnection at a downstream distance of $\gtrapprox$20 R_E. *Lopez and Lui* [1990] used observations from four satellites (Active Magnetospheric Particle Tracer Explorers (AMPTE)/CCE, AMPTE Ion Release Module, GOES 5, and GOES 6) in the near-Earth magnetotail region and ground magnetometers to demonstrate the tailward propagation of dipolarization. *Jacquey et al.* [1991] and *Jacquey et al.* [1993] investigated magnetic field perturbations in the tail lobe to infer tailward propagation of dipolarization. *Ohtani et al.* [1992] paid attention to the different sensitivities of B_z and B_x components to the cross-tail current to infer tailward propagation of dipolarization.

More recently, DFs are also thought to result from magnetic reconnection in which the exhaust jets and entrained magnetic fluxes from the reconnection region pileup, forming a front of increased current sheet normal magnetic field [*Hoshino et al.*, 2001; *Hoshino*, 2005; *Nakamura et al.*, 2009; *Sitnov et al.*, 2009]. Kinetic particle-in-cell simulations [*Sitnov et al.*, 2009] have shown that DFs can form as a result of transient reconnection.

In this paper, we report Cluster observations of consecutive sharp B_z jumps in the near-Earth current sheet. The initial thickness of the current sheet is comparable to the inertial length of H^+ ions. The two boundaries of sharp B_z jumps are separated by about 5 min; the earlier front propagates radially outward and is followed by a series of tailward moving flux ropes, consequently leaving the near-Earth plasma sheet to become further thinned. The later DF propagates earthward very rapidly (at a speed of ~542.5 km/s) and is associated with global magnetic dipolarization following the front. We investigate ground magnetometer data around the meridian of Cluster's foot points to track ionospheric responses to the localized fronts in the coupled ionosphere-magnetosphere current system. Two-step positive bay enhancements are observed; one of which started 3 min earlier than the Cluster observation of the first B_z enhancement and a second one that started 2 min after the DF detection by Cluster. A positive bay associated with the first B_z enhancement was seen at low latitudes before being observed at higher latitudes, indicating that the substorm onset signatures propagated from the inner plasma sheet to the outer plasma sheet, consistent with the Cluster observation of tailward propagating magnetic disturbances.

In the following section we present an overview of the DF events and examine magnetotail configuration and dynamics associated with these magnetic disturbances (section 2). Ground magnetometer data during this event are shown in section 3, where we also discuss how this event is related to the substorm onset mechanisms and dynamics.

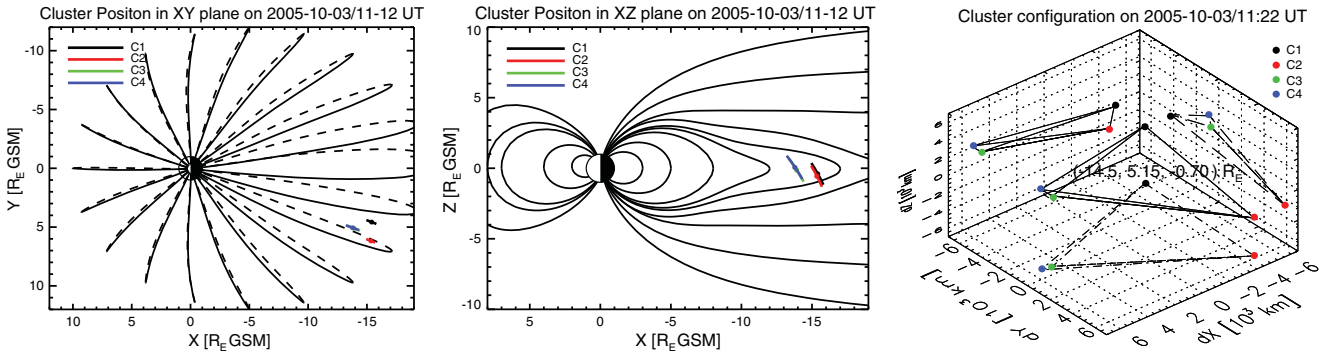

Figure 1. Location of the four Cluster spacecraft during 1100–1200 UT on 3 October 2005; in the GSM (left) *XY* and (middle) *XZ* planes, superposed over magnetic field lines obtained from the T96 model [*Tsyganenko*, 1995]. (right) The spacecraft configuration and separation at 1122 UT (the event start time) are shown. The barycenter of the four Cluster spacecraft is at (−14.5, 5.15, −0.70) Earth radii (R_E) in GSM coordinates.

2. Observations of Abrupt B_z Enhancements

2.1. Initial B_z Enhancement: Tailward Propagation

During 1100–1200 UT on 3 October 2005, the four Cluster spacecraft passed the premidnight sector of the near-Earth neutral sheet from north to south (Figure 1). The barycenter of the quartet was at (−14.5, 5.15, −0.70) Earth radii (R_E) in geocentric solar magnetospheric (GSM) coordinates. The separation between the spacecraft along the *z* direction, i.e., almost along the normal to the current sheet, is significantly smaller than is their separation in the *xy* plane. C3 and C4 are quite close to each other.

Cluster observations during 1120–1133 UT is summarized in Figure 2 that shows (a) negative of the spacecraft potential that is indicative of the electron density [*Pedersen et al.*, 2008; *Lybekk et al.*, 2012], (b–d) the (*x*, *y*, *z*) components of the magnetic field, and the ion bulk velocity measured by (e) C1 and (f) C4 (for H^+ ions). (No ion moments from C3 are available during the event.) Prior to the event, e.g., between 1120:00 and 1121:40 UT, B_x components are notably different among the four spacecraft, while all the B_z values are close to zero ($|B_z| \leq 2.5$ nT). The current sheet normal coordinates point along $\hat{l} = (0.96, 0.27, 0.13)$, $\hat{m} = (-0.16, 0.90, -0.41)$, and $\hat{n} = (-0.21, 0.37, 0.90)$ in GSM coordinates as obtained from the magnetic field measured by C1, which marginally traversed the current sheet at ~1122 UT. The medium-to-minimum eigenvalue ratio in the minimum variance calculation is 6.5 for ~2000 data points. The bootstrap error estimate for the minimum variance analysis [*Kawano and Higuchi*, 1995] shows a standard deviation of 0.026. We fit the magnetic field data at C1, C3, and C4 taken prior to detection of the large magnetic field fluctuations (starting at ~1122:10 UT) to a Harris sheet model, $B_l(n) = B_0 \tanh \frac{n-n_0}{L}$, where B_0 is lobe magnetic field outside the current sheet along $\hat{l}$, n_0 is current sheet position, and L is half thickness of the current sheet, with the result that the current sheet half thickness along $\hat{n}$ to range between 1498 km and 1802 km. These are comparable to the inertial length (~1000 km) or gyroradius (~1800 km) scale of H^+ ions, indicating that the near-Earth current sheet was thin before the event.

The magnetic field data at C2 neither fit the derived (*l*, *m*, *n*) coordinates nor are applicable for calculating the current sheet thickness. The magnetic field profiles at C2 that differ from other spacecraft data indicate that C2 resided in a different region topologically being away from the current sheet, although C2 was only ~0.35 R_E southward of C1 in GSM. Moreover, the large dawnward B_y component at ~1122 UT measured by C2 suggests that the background magnetic field surrounding the central current sheet was stretched dawnward prior to the event so that the other three spacecraft were aligned in the same magnetic meridian plane, although the model magnetic field [*Tsyganenko*, 1995] (see Figure 1) predicted that C2 and C3/C4 should be in nearly the same meridian.

At ~1122:12 UT, C3 and C4 observed an abrupt jump in B_z while C1 observed a bit more gradual increase of B_z ~26 s later (marked by cyan and grey arrows, respectively, in Figure 2d). The earthward plasma flow observed at C4 (Figure 2f) starts before the enhanced B_z front and peaks at 1100 km/s 12.6 s later (at ~1122:24.6 UT) passing the front (cyan arrow in Figure 2f; note that there are no ion moments for C3 during this event). The peak of earthward fast flow at C1 (~660 km/s at ~1122:39 UT, grey arrow in Figure 2e) almost coincides with the B_z enhancement. C2 did not observe the B_z jump and the magnetic field profiles

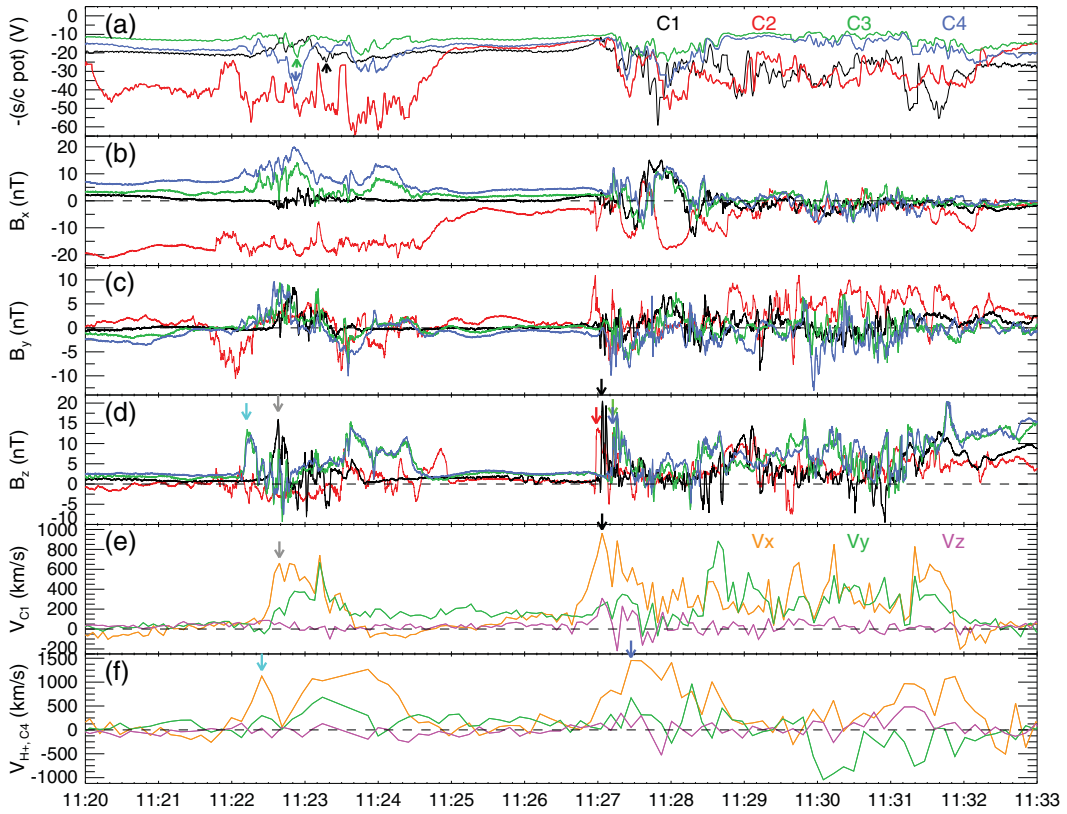

Figure 2. Cluster observations of two consecutive B_z enhancements on 3 October 2005: (a) the negative of the spacecraft potential, indicative of the electron density [*Pedersen et al.*, 2008; *Lybekk et al.*, 2012]; the magnetic field, (b) B_x, (c) B_y, and (d) B_z; (e, f) the ion bulk flow, V_x (orange), V_y (green), and V_z (magenta) measured at C1 (Figure 2e) and C4 (Figure 2f, assuming that the majority is H^+ ions).

between C3/C4 and C1 are not very similar, meaning that reliable multispacecraft timing analyses cannot be performed. However, the data show a consistent trend, viz. that fluctuations propagate radially outward, i.e., from C3/C4 to C1: (1) the sudden B_z increases accompanying earthward fast flows (Figures 2d–2f), (2) local density decreases detected ~40 s after the B_z jump (arrows in Figure 2a), and (3) the ~50 s long B_x fluctuations at ~0.15 Hz around or following the B_z jump (Figure 2b) are all observed at C3/C4 first, and then at C1 later, by ~26 s apart.

Increasing $\bar{B}_x$ (the mean magnitude of B_x) with decreasing $\bar{B}_z$ following the B_z enhancement (~1122:20–1122:50 UT for C3/C4 and ~1122:40–1123:05 UT for C1) indicates that the local B_z jump led to a more stretched current sheet, which is opposite to the more usual observation, where the DF appears as an interface formed by earthward injected flux tubes that contain more dipole magnetic field components than did the preexisting flux tubes. Note that a second B_z jump passed all four spacecraft ~5 min later (marked by red, black, green, and red arrows in Figure 2d). This second event is discussed in detail in section 2.2.

We expand the period of the first enhanced B_z front crossing in Figure 3, where the magnetic field components (a–c), the current (d) calculated assuming that the spatial derivatives are replaced by temporal ones using the spacecraft velocity $\left(\frac{dB_i}{dx_j} = \frac{1}{V_{s/c,j}}\frac{dB_i}{dt}\right)$, the bulk plasma velocity (e, f), and the electric field components (g–i) are shown in the current sheet normal coordinates. The magnetic field profiles reveal that the ~0.15 Hz fluctuations following the B_z jump correspond to a series of flux ropes that move tailward: (1) Enhancements in positive B_m and J_m (Figures 3b and 3d) mostly occur when bipolar B_n changes its sign from positive to negative (marked by dotted, dash-dotted, and dashed vertical lines for C1, C3, and C4; see Figure 3c). (2) Local enhancements in B_l (Figure 3a) coincide with negative-to-positive B_n changes (see the cartoon in Figure 4 that indicates a relative spacecraft trajectory passing the tailward moving flux ropes/plasmoids). The timings for the spacecraft to approach closest to the center of the flux ropes are

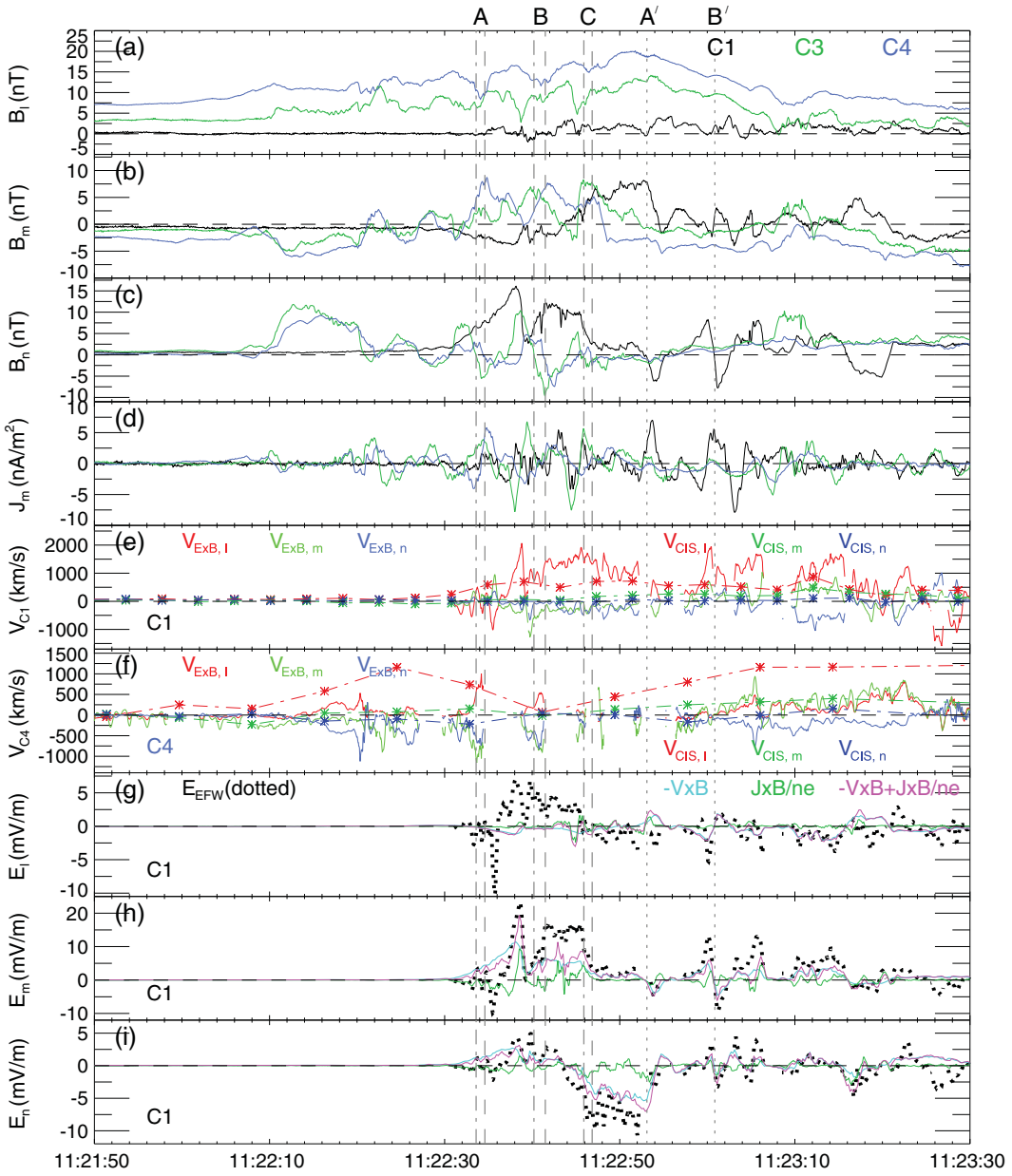

Figure 3. Expanded for the period of the first B_z enhancement crossing with all parameters in the current sheet normal coordinates; (a–c) the magnetic field components, (d) the current along $\hat{m}$ direction, calculated assuming that the spatial derivatives are replaced by temporal ones using the spacecraft velocity $\left(\frac{dB_i}{dx_j} = \frac{dB_i}{V_{j,s/c}dt}\right)$, (e, f) the bulk plasma velocity at C1 and C4, and (g–i) the electric field at C1. The bulk plasma velocities measured by Cluster-CIS (Cluster Ion Spectrometry) are compared with the frozen-in convection flows (Figures 3e and 3f). Figures 3g–3i show contributions of the convection term (cyan) and the Hall term (green), separately, and compare the sum of the two terms (magenta) to the measured electric field (black dotted). Dotted, dash-dotted, and dashed vertical lines for C1, C3, and C4, respectively, represent when B_n changes its sign from positive to negative as tailward moving flux ropes pass the spacecraft.

marked by A and B for C3 and C4, and A′ and B′ for C1 in the cartoon of Figure 4, corresponding to the ones (shown at the top of Figure 3), around which B_n changes its sign.

Figure 4 demonstrates that a single period among the multiple bipolar B_n structures can be well fitted to a force-free flux rope model, where $\mu_0\mathbf{J} = \alpha\mathbf{B}$ (so that $\mathbf{J} \times \mathbf{B} = 0$). For a constant α, Ampere's law becomes a Helmholtz equation whose solutions are Bessel functions [*Lundquist*, 1950]. The flux rope in a force-free configuration has cylindrical symmetry, represented by the axial (B_A), tangential (B_T), and radial (B_R)

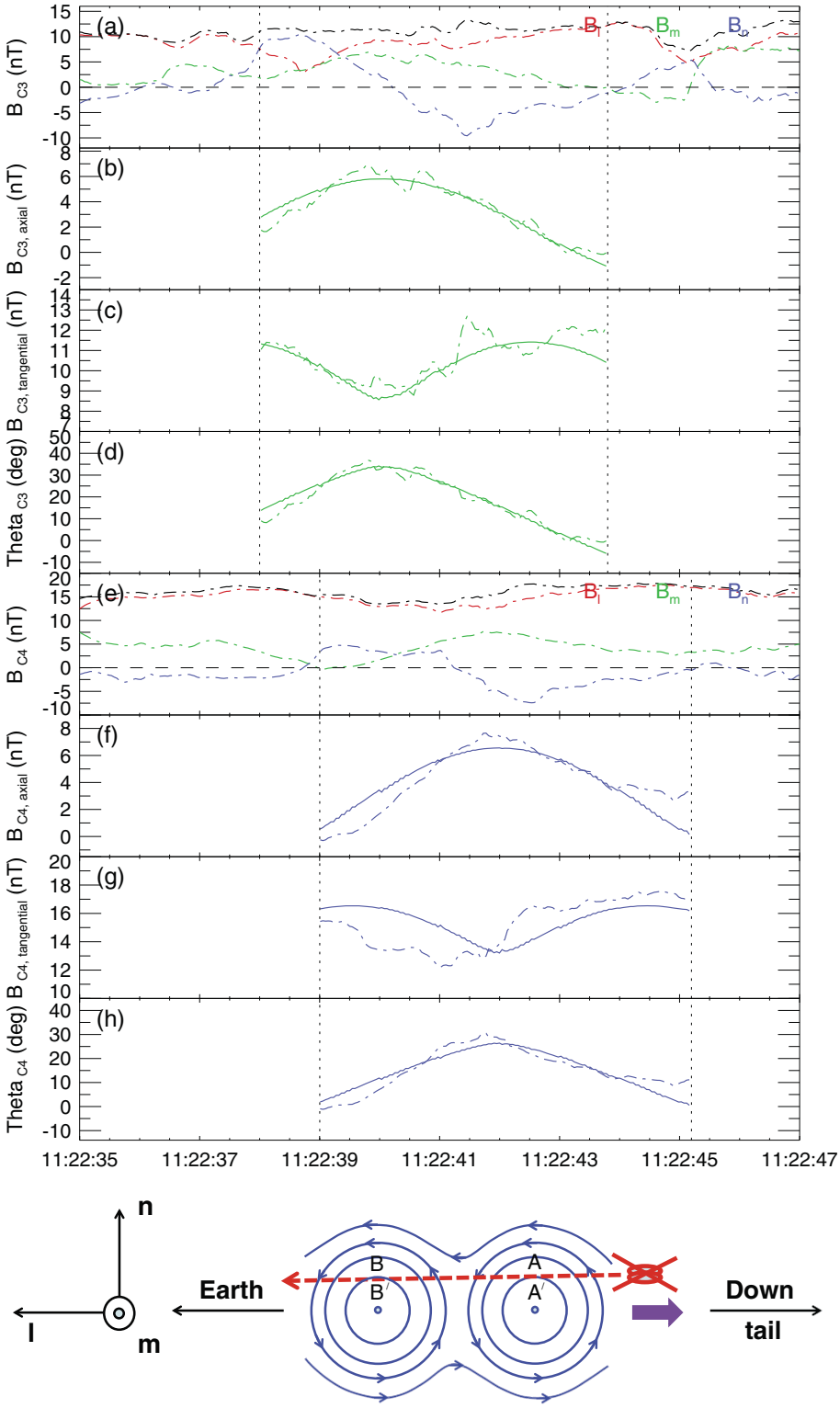

Figure 4. A single period among a series of bipolar-B_n structures. The measured magnetic fields (dot-dashed curves) are fitted to force-free flux rope model predictions (solid curves) for (a–d) C3 and (e–h) C4: Axial (Figures 4b and 4f) and tangential (Figures 4c and 4g) components, and the angle (Figures 4d and 4h) made by the axial component to the total magnetic strength (with 90° corresponding to the core of the flux rope). The bottom cartoon illustrates Cluster's crossing of multiple tailward moving flux ropes. The timings for the spacecraft to pass closest to the center of the flux ropes are marked by A and B for C3 and C4, and A′ and B′ for C1, corresponding to the ones (shown at the top of Figure 3), around which timings B_n changes its sign.

components of the magnetic field: $B_A = B_0 J_0(aR)$, $B_T = B_0 H J_1(aR)$, and $B_R = 0$, where R is the distance from the axis, $H = \pm 1$ determines the handedness of the magnetic field, and B_0 and a are constants determined by the fit. Figure 4 shows axial (b, f) and tangential (c, g) components, and the angle (d, h) made by the axial component to the total magnetic strength (with 90° corresponding to the core of the flux rope) observed at C3 and C4 (dash-dotted curves in Figures 4a–4d and 4e–4h, respectively). Overplotted are the model values shown in solid curves. B_0 and a in our fit are 21.9 nT and 14.29 R_E^{-1} (26.5 nT and 15.04 R_E^{-1}) with a standard deviation of 0.079 and 0.010 (0.094 and 0.011), respectively, for C3 (C4). Both C3 and C4 show good consistency between the measurements and the model predictions, while C1 data (not shown) are less consistent, indicating the slight deformation of the flux ropes, similar to the enhanced B_z (B_n) front.

Two-point timings between C3 and C1 using either the B_z jumps or the two sharp negative B_n dips associated with flux ropes (Figure 3c) yield an estimate for the velocity of these structures as 399–519 km/s to the negative (tailward) $\hat{l}$ direction. The scale sizes along $\hat{l}$ of a single flux rope (with an average duration of 6.5 s) are estimated to be 2594–3374 km (0.4–0.53 R_E). To test whether or not the criteria for the tearing instability ($k \cdot \Delta \leq 1$, where k is the wave number associated with the spacing along $\hat{l}$ of the inferred tearing-mode structure and Δ is the thickness of the initial current sheet) [*Furth et al.*, 1963; *Coppi et al.*, 1966] were met, we assume that the scale size of a flux rope along $\hat{l}$ (suggesting the separation of the two X lines along $\hat{l}$) is an estimate of the wavelength of the initial mode (λ). Using the thickness of the initial current sheet (Δ) obtained from the Harris model gives $k \cdot \Delta = (2\pi/\lambda) \cdot \Delta = 5.6$–$8.6$. The two-point timing method might have overestimated the propagation speed and therefore scale sizes of the flux ropes. The force-free flux rope model fitted to the data also gives the diameter of the flux rope as 0.34 R_E (for C3) and 0.32 R_E (C4). This implies that $k \cdot \Delta$ can be even larger. Therefore, the tearing instability seemed unlikely to generate a series of flux ropes during the first enhanced B_z event.

Tailward propagation of both the B_z enhancements and the following flux ropes during the earthward plasma bulk flows (Figures 2e and 2f) indicates a breakdown in the frozen-in condition. Figures 3e and 3f compare velocity components obtained by the electric and magnetic fields ($\frac{\mathbf{E}\times\mathbf{B}}{B^2}$; red, green, and blue curves representing *l*, *m*, and *n* components) and Cluster-CIS instruments (dark red, dark green, and dark blue dash-dotted curves with asterisks pointing measurement times). Despite much lower resolution of ion moments (4 s for C1 and 8 s for C4) compared to the field data and intermittent unavailability of the electric field data, notable differences between the two measurements are clear. Figures 3g–3i detail relative contributions by the convection ($-\mathbf{V} \times \mathbf{B}$) and Hall ($\mathbf{J} \times \mathbf{B}/ne$) terms in the generalized Ohm's law, $\mathbf{E} = -\mathbf{V} \times \mathbf{B} + \mathbf{J} \times \mathbf{B}/ne - \nabla \cdot \overleftrightarrow{\mathbf{P}_\mathbf{e}}/ne + \frac{m_e}{ne^2}\frac{\mathrm{d}\mathbf{J}}{\mathrm{d}t} + \eta\mathbf{J}$ [*Yoon and Lui*, 2006]. The plot uses data from C1, which provides the highest resolution ion moments. The relatively poor data cadence available for electron moments (1 sampling per ≥70 s for C1) does not allow us to consider the third term, called the electron pressure (electron viscosity) term. The fourth term, i.e., the electron inertial term, is insignificant in the present event (not shown). Figures 3g–3i indicate that both the convection and Hall terms (cyan and green curves, respectively) significantly contribute around the B_n enhancement to balance the measured electric field (dotted), while the convection terms are dominant during the passage of a series of flux ropes (as expected for the force-free flux ropes). However, the sums of the two terms displayed in magenta curves show a poor agreement to the measured fields near the rise of the B_n enhancement, the B_n plateau during 1122:41.7–46 UT, and bipolar *n* peaks associated with flux ropes. This indicates that either the electron viscosity term which becomes important when the electron pressure tensor contains large off-diagonal components or the anomalous resistivity ($\eta\mathbf{J}$) which arises from turbulent field fluctuations [*Lui et al.*, 2007] might have significantly contributed. Indeed, off-diagonal components in the electron pressure tensor during the flux rope passage are less than diagonal ones by about an order of magnitude, compared to more notable differences by 2–3 orders of magnitude for other times.

2.2. Later B_z Enhancement: Earthward Propagation

At ~1127 UT, i.e., about 5 min after the initial B_z enhancement, a second B_z jump passed the four spacecraft (Figure 2d). The arrival of a DF is observed sequentially by C2, C1, C4, and C3. Figure 5 expands this period, using the same format as Figure 2 except that the spacecraft potential in Figure 5a is replaced by the electron density estimated from the spacecraft potential using *Lybekk et al.* [2012]. Prior to the B_z jump, all spacecraft were located close to the current sheet, with C1/C3/C4 on the northern side of the current sheet while C2 in the southern side observing stretched field lines along the $+\hat{y}$ direction (Figures 5b–5d). An abrupt B_z increase, marked by colored arrows in Figure 5d is preceded by a typical B_z dip ahead of it. A notable difference of the DF observations among the spacecraft is that the DF forms as a single B_z rise at

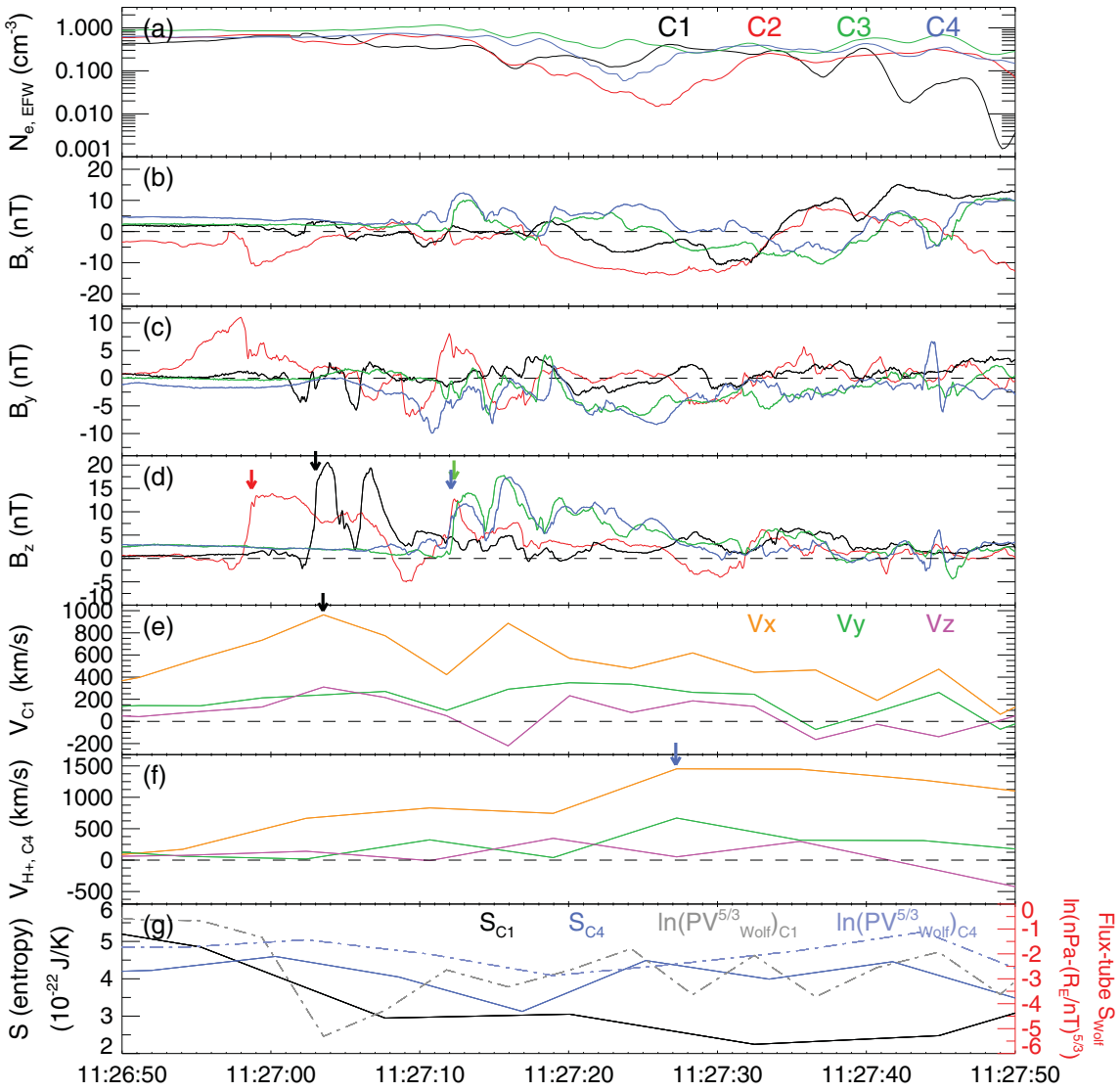

Figure 5. Detailed profiles of the (a) electron density, estimated from the spacecraft potential using *Lybekk et al.* [2012], (b–d) magnetic field components, plasma bulk velocities measured by (e) C1 and (f) C4, and entropy calculated from the ion distribution function (solid black and blue lines for C1 and C4, respectively) or the flux tube entropy parameter (using *Wolf et al.* [2006]'s formula, dash-dotted grey and light blue lines for C1 and C4) (g) during the passage of the later B_z enhancement.

C2 while it is seen as a double rise at C1 or multiple rises at C3 and C4 later with time. This indicates either that the front was bifurcated consecutively due to kinetic processes occurring at the DF or that recurrent bursty magnetic reconnection injected multiple outflowing reconnected flux tubes into the inner plasma sheet. Figures 5e and 5f show that the DF observed at C1 and C4 accompanies multiple-peaked earthward fast flows, possibly supporting the latter scenario. In particular, the later earthward flow speed at C4 (marked by a blue arrow in Figure 5f) is about 1.6 times the earlier one seen at ~1127:10 UT. This might correspond to the larger B_z rise detected later at ~1127:15.5 UT as being generated by larger compressions due to faster earthward flows. Four-spacecraft analysis using timings of the first rise of B_z jumps (red, black, blue, and green arrows in Figure 5d) gives the normal propagation of the front to be ~542.5 km/s along (0.75, −0.39, −0.53) in GSM coordinates (almost identical to LMN coordinates during the later front period). The four-spacecraft timing analysis assumes that the boundary front is nearly planar and quasi-stationary, which is often satisfied for DFs. The technique also assumes that the front moves with constant velocity over the scale of the spacecraft separation. Two-point timings using C1 and C3/C4 observations overestimate the speed as ~770 km/s in GSM/LMN. Therefore, the later DF propagated earthward significantly faster than the tailward motion of the initial B_z enhancement.

Figure 5g shows the entropy calculated from the ion distribution function (solid black and blue lines for C1 and C4, respectively) [*Hwang et al.*, 2011] or the flux tube entropy parameter using *Wolf et al.* [2006]'s formula (dash-dotted grey and light blue lines for C1 and C4). Despite unfavorable temporal resolution of the ion distributions and moments, one can see a decrease in the entropy during the passage of the later B_z enhancement, in particular for C1, which is situated in closer proximity to the neutral sheet than C4, as indicated from the magnetic field components prior to the B_z enhancement. The decrease in the (flux tube) entropy could be linked to the fast propagation of the later DF.

3. Discussion

We report Cluster observations of two consecutive B_z enhancements separated in time by ~5 min. The first B_z jump and subsequent flux ropes, both propagating tailward, seem to be associated with non-MHD and non-reconnection processes while the second event propagates rapidly earthward and is consistent with generation via magnetotail reconnection. Between the two B_z enhancements (during 1125:00–1126:50 UT in Figure 2), the current sheet shows a reduction in magnetic flux (in which $|B|$ decreased to ~25%, 64%, and 49% of before-the-event levels for C2, C3, and C4, respectively). This indicates that the tailward moving first B_z enhancement together with a series of flux rope structures resulted in a significant removal of magnetic flux from the near-Earth plasma sheet outward to the distant tail. This leads the magnetotail to be globally stretched so that the thinnest current sheet forms tailward of the location of Cluster's detection of the first B_z jump. The region of the most thinned current sheet facilitates magnetic reconnection that quickly evolves from the plasma sheet to the lobe field reconnection, which can generate a rapid earthward propagating DF associated with a large decrease in plasma density and flux tube entropy within reconnected flux tubes behind the DF. Figure 2a and Figure 5a show a significant density decrease of 2 orders of magnitude after the passage of the later front. Figure 5g also indicates a large (flux tube) entropy decrease behind the later DF. This series of magnetotail processes will likely lead to subsequent dipolarization of magnetotail topology, which is observed by Cluster near the end of the event (see the reduced B_x with enhanced B_z in Figures 2b and 2d after 1132:15 UT).

This scenario of the near-Earth tail dynamics suggests that the two consecutive B_z enhancements are causally linked. This relationship may be represented by ionospheric responses to the two B_z jumps and their outward/inward motions. Black, red, green, and blue traces in Figure 6 (top) are the footprints of the Cluster spacecraft as derived from T96 [*Tsyganenko*, 1995] during 1100 to 1200 UT, with dots corresponding to the footprints at 1122 UT. Geocentric longitudes and latitudes of C1 are −176° and 72.2° at 1122 UT and −179° and 72.5° at 1127 UT. Below are panels that show northward (H), eastward (D), and vertical (Z) components of ground-based magnetometer data recorded at four stations marked in the map. (Note that for this event, all-sky imaging data are unavailable.) The magnetogram from the IRT station displays clear features of a two-step positive bay. The initial one starts at ~1119 UT (marked by a hollow magenta arrow), i.e., ~3 min prior to the traverse of the first B_z enhancement through Cluster. The later one starts at ~1129 UT (marked by a solid magenta arrow), ~2 min after the second B_z jump was seen at Cluster. These positive bays are associated with the upward, i.e., tailward, field-aligned currents on the western side of the substorm current wedge [*Atkinson*, 1967; *McPherron et al.*, 1973]. Around the time of the first B_z enhancement at Cluster (~1122 UT), we see a positive bay features at the lower latitudes (MMB starting at ~1118 UT and IRT at ~1119 UT) before it is observed at the higher latitudes at CHD (~1121:30 UT) and KTN (~1122:30 UT), which is consistent to the tailward motion of the first B_z enhancement. Around the time of the later earthward DF event observed by Cluster at ~1127 UT, a negative bay, starting at ~1124 UT at KTN and reversed from having been positive at ~1125 UT at CHD, continues until ~1132 UT (KTN) and ~1133:30 UT (CHD). A weaker negative bay appears during 1126–1129 UT at IRT and 1128–1129 UT at MMB. More dominant positive bays start at ~1129 UT and last until ~1135 UT as seen at IRT/MMB. In particular, between ~1129 and 1132 UT, the higher latitude stations (KTN and CHD) observe a negative bay while lower latitude stations see a positive bay. This indicates that the westward substorm electrojet developed somewhere between CHD and IRT/MMB stations. These bay features demonstrate that the westward auroral electroject, which formed northward of the four stations (tailward of the location mapped to the magnetotail), propagates to the lower latitudes (earthward in the magnetotail), consistent with the earthward motion of the second DF. Although the two positive bays observed at IRT might represent separate substorms, the later one shows larger variations with wider and prolonged impacts (over all four stations). This, together with the fact that substorms

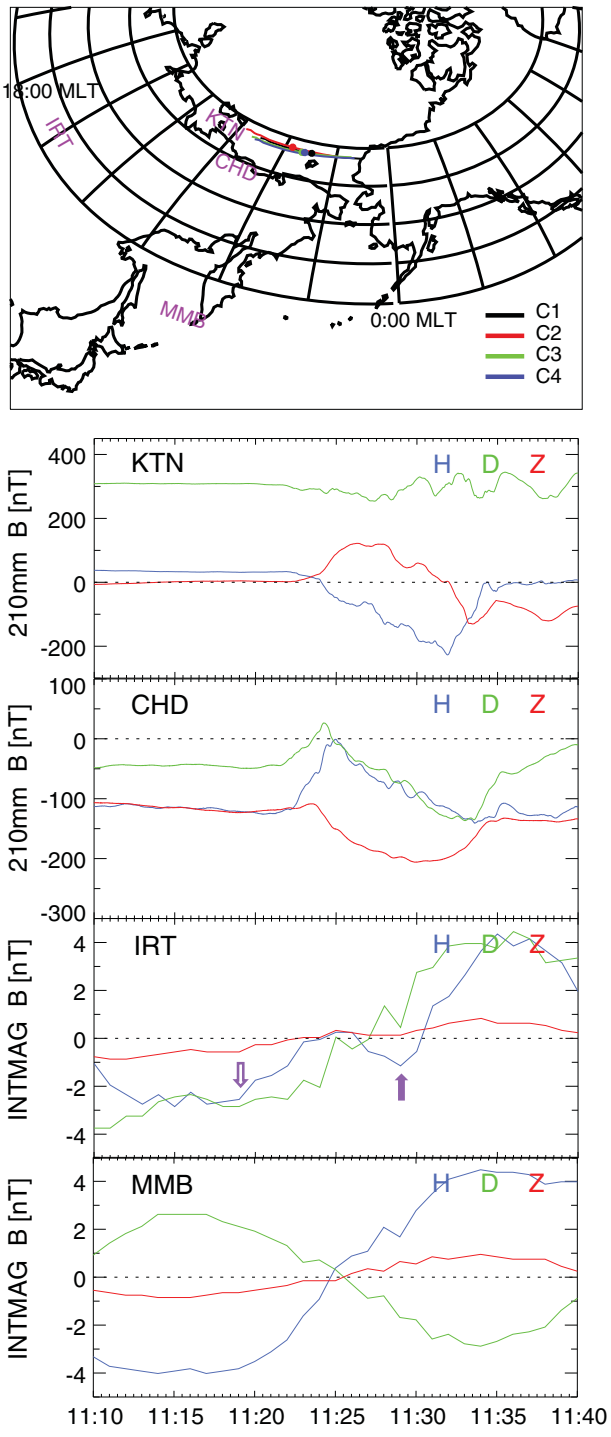

Figure 6. Ground magnetograms observed at four stations (KTN, CHD, IRT, and MMB) located around the meridian of (top) Cluster's foot points that are marked in the map.

are unlikely to last less than 5 min suggests that the initial variations are associated with preconditioning of a later strong substorm enhancement.

Both in situ observations in the near-Earth tail and magnetometer measurements on the ground correlate to the cross-tail current disruption model [*Lui*, 1991] in that the current disrupted structures propagating tailward (corresponding to the initial B_z enhancement) coincide with earthward plasma flows and that signatures indicative of tailward reconnection (corresponding to the later B_z enhancement) shortly follows being associated with (stronger) substorm. The current disruption model attributes the abrupt disturbances in the near-Earth current sheet to the cross-tail current instability [*Lui et al.*, 1991], which evacuates plasmas tailward of the disrupted region by the convection surge, giving rise to earthward bulk flows to fill up the evacuated region together with tailward moving rarefaction waves [*Lui*, 1991]. Such rarefaction waves may serve as a trigger for midtail reconnection in the current disruption model. Figure 2 shows that a density dip (marked by arrows in Figure 2a) appears shortly after the peak of earthward fast flows (Figures 2e and 2f) and propagates tailward. Ionospheric responses also correspond well to the substorm onset signatures propagating from the inner plasma sheet to the outer plasma sheet, consistent with the Cluster observations. The sequence of events suggests strongly that the first event may have been a different form of current disruption that originated near Earth and propagated tailward, triggering or facilitating midtail reconnection, thereby serving to precondition the magnetosphere for a later strong substorm enhancement.

4. Conclusions

We presented a case study detected by the Cluster spacecraft and ground-based magnetometers that shows substorm onset propagating from the inner plasma sheet to the outer plasma sheet. When the spacecraft traversed a thin current sheet of thickness comparable to the ion inertial length, sudden enhancements of the z component of the magnetic field were consecutively observed ~5 min apart. The initial B_z enhancement and a series of flux rope structures that immediately followed by the local B_z enhancement propagated tailward. Along with those structures, there was a region of rarefied plasma that

also moved tailward. The later B_z enhancement, featuring a typical dipolarization front, was observed to rapidly propagate earthward at the speed of ~542.5 km/s and is followed by a large density and flux tube entropy decrease. Between the two B_z enhancements, the current sheet experienced significant removal of magnetic flux from the near-Earth plasma sheet, possibly out to the distant tail, associated with the tailward moving B_z enhancement and flux rope structures. The sequence of observations indicates that the magnetic flux removal caused the magnetotail to be globally stretched so that the thinnest region of the current sheet formed tailward of Cluster. The thinned current sheet, then, would likely facilitate magnetic reconnection that quickly evolved from the plasma sheet to the magnetotail lobe and generated a rapid earthward moving DF that was followed by a significant reduction in density and entropy, as was observed by Cluster. Ground magnetograms located near the meridian of Cluster's magnetic foot points show two-step positive bay enhancements; one of which started 3 min earlier than the Cluster observation of the initial B_z enhancement in the near-Earth plasma sheet and the later one started 2 min after the later DF detection by Cluster. A positive bay associated with the first B_z enhancement was seen at low latitudes before being observed at higher latitudes, indicating that the substorm onset signatures propagated from the inner plasma sheet to the outer plasma sheet, consistent with the Cluster observation of tailward propagating magnetic disturbances and rarefaction waves. More intense negative and positive bay features associated with the later B_z enhancement form northward of the magnetometer stations and propagate to the lower latitudes, also consistent with the earthward motion of the later DF. The present event highly suggests that the current disruption signatures that originated in the near-Earth current sheet propagated tailward, triggering or facilitating midtail reconnection, thereby preconditioning the magnetosphere for a later strong substorm enhancement.

Acknowledgments

K.J.H. and M.L.G. were supported, in part, by NASA's Magnetospheric Multiscale Mission Interdisciplinary Science (MMS/IDS) grant to the Goddard Space Flight Center and by the Cluster mission. T.E.M. participated with support from the MMS Mission. This work was partly supported by SB RAS project 106 and RFBR grant 12-05-98522 and RFBR grant 13-05-00363 (MAV). K.J.H. was supported, in part, by NASA grant NNH12ZDA001N-GEO. K.J.H. appreciates useful comments by H. Kawano.

Michael Liemohn thanks the reviewers for their assistance in evaluating this paper.

References

Angelopoulos, V., W. Baumjohann, C. F. Kennel, F. V. Coroniti, M. G. Kivelson, R. Pellat, R. J. Walker, H. Lühr, and G. Paschmann (1992), Bursty bulk flows in the inner central plasma sheet, *J. Geophys. Res.*, *97*, 4027–4039.

Angelopoulos, V., F. S. Mozer, T. Mukai, K. Tsuruda, S. Kokubun, and T. J. Hughes (1999), On the relationship between bursty flows, current disruption and substorms, *Geophys. Res. Lett.*, *26*, 2841–2844.

Ashour-Abdalla, M., M. El-Alaoui, M. L. Goldstein, M. Zhou, D. Schriver, R. Richard, R. Walker, M. G. Kivelson, and K.-J. Hwang (2011), Observations and simulations of non-local acceleration of electrons in magnetotail magnetic reconnection events, nature physics, *Nat. Phys.*, *7*, 360–365, doi:10.1038/nphys1903.

Atkinson, G. (1967), An approximate flow equation for geomagnetic flux tubes and its application to polar substorms, *J. Geophys. Res.*, *72*, 5373–5382.

Birn, J., J. Raeder, Y. L. Wang, R. A. Wolf, and M. Hesse (2003), On the propagation of bubbles in the geomagnetic tail, *Ann. Geophys.*, *22*, 1773–1786.

Birn, J., M. Hesse, R. Nakamura, and S. Zaharia (2013), Particle acceleration in dipolarization events, *J. Geophys. Res. Space Physics*, *118*, 1960–1971, doi:10.1002/jgra.50132.

Coppi, B., G. Laval, and R. Pellat (1966), Dynamics of the geomagnetic tail, *Phys. Rev. Lett.*, *16*, 1207–1210.

Delcourt, D. C. (2002), Particle acceleration by inductive electric fields in the inner magnetosphere, *J. Atmos. Sol. Terr. Phys.*, *64*, 551–559.

Delcourt, D. C., A. Pedersen, and J. A. Sauvaud (1990), Dynamics of single-particle orbits during substorm expansion phase, *J. Geophys. Res.*, *95*, 20,853–20,865.

Deng, X., M. Ashour-Abdalla, M. Zhou, R. Walker, M. El-Alaoui, V. Angelopoulos, R. E. Ergun, and D. Schriver (2010), Wave and particle characteristics of earthward electron injections associated with dipolarization fronts, *J. Geophys. Res.*, *115*, A09225, doi:10.1029/2009JA015107.

Dubyagin, S., V. Sergeev, S. Apatenkov, V. Angelopoulos, R. Nakamura, J. McFadden, D. Larson, and J. Bonnell (2010), Pressure and entropy changes in the flow-braking region during magnetic field dipolarization, *J. Geophys. Res.*, *115*, A10225, doi:10.1029/2010JA015625.

Fok, M.-C., T. E. Moore, P. C. Brandt, D. C. Delcourt, S. P. Slinker, and J. A. Fedder (2006), Impulsive enhancements of oxygen ions during substorms, *J. Geophys. Res.*, *111*, A10222, doi:10.1029/2006JA011839.

Fu, H. S., Y. V. Khotyaintsev, M. André, and A. Vaivads (2011), Fermi and betatron acceleration of suprathermal electrons behind dipolarization fronts, *Geophys. Res. Lett.*, *38*, L16104, doi:10.1029/2011GL048528.

Fu, H. S., Y. V. Khotyaintsev, A. Vaivads, M. André, and S. Y. Huang (2012), Occurrence rate of earthward-propagating dipolarization fronts, *Geophys. Res. Lett.*, *39*, L10101, doi:10.1029/2012GL051784.

Furth, H. P., K. Kileen, and M. N. Rosenbluth (1963), Finite-resistivity instabilities of a sheet pinch, *Phys. Fluids*, *6*, 459.

Ge, Y. S., X.-Z. Zhou, J. Liang, J. Raeder, M. L. Gilson, E. Donovan, V. Angelopoulos, and A. Runov (2012), Dipolarization fronts and associated auroral activities: 1. Conjugate observations and perspectives from global MHD simulations, *J. Geophys. Res.*, *117*, A10226, doi:10.1029/2012JA017676.

Hoshino, M. (2005), Electron surfing acceleration in magnetic reconnection, *J. Geophys. Res.*, *110*, A10215, doi:10.1029/2005JA011229.

Hoshino, M., T. Mukai, T. Terasawa, and I. Shinohara (2001), Superthermal electron acceleration in magnetic reconnection, *J. Geophys. Res.*, *106*, 25,972.

Hwang, K.-J., M. L. Goldstein, E. Lee, and J. S. Pickett (2011), Cluster observations of multiple dipolarization fronts, *J. Geophys. Res.*, *116*, A00I32, doi:10.1029/2010JA015742.

Hwang, K.-J., M. L. Goldstein, A. F.-Viñas, D. Schriver, and M. Ashour-Abdalla (2014), Wave-particle interactions during a dipolarization event, *J. Geophys. Res. Space Physics*, *119*, 2484–2493, doi:10.1002/2013JA019259.

Jacquey, C., J. A. Sauvaud, and J. Dandouras (1991), Location and propagation of the magnetotail current disruption during substorm expansion: Analysis and simulation of an ISEE multi-onset event, *Geophys. Res. Lett.*, *18*, 18,389–18,392.

Jacquey, C., J. A. Sauvaud, J. Dandouras, and A. Korth (1993), Tailward propagating cross-tail current disruption and dynamics of near-Earth tail: A multi-point measurement analysis, *Geophys. Res. Lett.*, *20*, 983–986.

Jones, S. T., M. Fok, and P. C. Brandt (2006), Modeling global O^+ substorm injection using analytic magnetic field model, *J. Geophys. Res.*, *111*, A11S07, doi:10.1029/2006JA011607.

Kawano, H., and T. Higuchi (1995), The bootstrap method in space physics: Error estimation for the minimum-variance analysis, *Geophys. Res. Lett.*, *22*, 307–310.

Keika, K., P. C. Brandt, S. Ohtani, D. G. Mitchell, K. Min, M. Nosé, T. Obara, H. Koshiishi, and H. Matsumoto (2010), Mass-dependent evolution of energetic neutral atoms energy spectra during storm time substorms: Implication for O^+ nonadiabatic acceleration, *J. Geophys. Res.*, *115*, A00I12, doi:10.1029/2010JA015889.

Lopez, R. E., and A. T. Y. Lui (1990), A multisatellite case study of the expansion of a substorm current wedge in the near-Earth magnetotail, *J. Geophys. Res.*, *95*, 8009–8017.

Lui, A. T. Y. (1991), A synthesis of magnetospheric substorm models, *J. Geophys. Res.*, *96*, 1849–1856.

Lui, A. T. Y., C.-L. Chang, A. Mankofsky, H.-K. Wong, and D. Winske (1991), A cross-field current instability for substorm expansions, *J. Geophys. Res.*, *96*, 11,389–11,401.

Lui, A. T. Y., Y. Zheng, H. Réme, M. W. Dunlop, G. Gustafsson, and C. J. Owen (2007), Breakdown of the frozen-in condition in the Earth's magnetotail, *J. Geophys. Res.*, *112*, A04215, doi:10.1029/2006JA012000.

Lundquist, S. (1950), Magnetohydrostatic fields, *Ark. Fys.*, *2*, 361.

Lybekk, B., A. Pedersen, S. Haaland, K. Svenes, A. N. Fazakerley, A. Masson, M. G. G. T. Taylor, and J.-G. Trotignon (2012), Solar cycle variations of the Cluster spacecraft potential and its use for electron density estimations, *J. Geophys. Res.*, *117*, A01217, doi:10.1029/2011JA016969.

McPherron, R. L., C. T. Russell, and M. Aubry (1973), Satellite studies of magnetospheric substorms on August 15, 1978: 9. Phenomenological model for substorms, *J. Geophys. Res.*, *78*, 3131–3149.

Nakamura, R., et al. (2002), Motion of the dipolarization front during a flow burst event observed by Cluster, *Geophys. Res. Lett.*, *29*(20), 1942, doi:10.1029/2002GL015763.

Nakamura, R., et al. (2009), Evolution of dipolarization in the near-Earth current sheet induced by earthward rapid flux transport, *Ann. Geophys.*, *27*, 1743–1754.

Nakamura, R., et al. (2011), Flux transport, dipolarization and current sheet evolution during a double-onset substorm, *J. Geophys. Res.*, *116*, A00I36, doi:10.1029/2010JA015865.

Nosé, M., H. Koshiishi, H. Matsumoto, P. C. Brandt, K. Keika, K. Koga, T. Goka, and T. Obara (2010), Magnetic field dipolarization in the deep inner magnetosphere and its role in development of O^+-rich ring current, *J. Geophys. Res.*, *115*, A00J03, doi:10.1029/2010JA015321.

Ohtani, S., K. Takahashi, and C. T. Russell (1992), Radial expansion of the tail current disruption during substorms: A new approach to substorm onset region, *J. Geophys. Res.*, *97*, 3129–3136.

Ohtani, S., P. C. Brandt, D. G. Mitchell, H. Singer, M. Nosé, G. D. Reeves, and S. B. Mende (2005), Storm-substorm relationship: Variations of the hydrogen and oxygen energetic neutral atom intensities during storm-time substorms, *J. Geophys. Res.*, *110*, A07219, doi:10.1029/2004JA010954.

Pedersen, A., et al. (2008), Electron density estimations derived from spacecraft potential measurements on Cluster in tenuous plasma regions, *J. Geophys. Res.*, *113*, A07S33, doi:10.1029/2007JA012636.

Runov, A., V. Angelopoulos, M. I. Sitnov, V. A. Sergeev, J. Bonnell, J. P. McFadden, D. Larson, K.-H. Glassmeier, and U. Auster (2009), THEMIS observations of an earthward-propagating dipolarization front, *Geophys. Res. Lett.*, *36*, L14106, doi:10.1029/2009GL038980.

Schmid, D., M. Volwerk, R. Nakamura, W. Baumjohann, and M. Heyn (2012), A statistical and event study of magnetotail dipolarization fronts, *Ann. Geophys.*, *29*, 1537–1547.

Sergeev, V., V. Angelopoulos, S. Apatenkov, J. Bonnell, R. Ergun, R. Nakamura, J. McFadden, D. Larson, and A. Runov (2009), Kinetic structure of the sharp injection/dipolarization front in the flow-braking region, *Geophys. Res. Lett.*, *36*, L21105, doi:10.1029/2009GL040658.

Sergeev, V. A., V. Angelopoulos, and R. Nakamura (2012), Recent advances in understanding substorm dynamics, *Geophys. Res. Lett.*, *39*, L05101, doi:10.1029/2012GL050859.

Sitnov, M. I., M. Swisdak, and A. V. Divin (2009), Dipolarization fronts as a signature of transient reconnection in the magnetotail, *J. Geophys. Res.*, *114*, A04202, doi:10.1029/2008JA013980.

Tsyganenko, N. A. (1995), Modeling the Earth's magnetospheric magnetic field confined within a realistic magnetopause, *J. Geophys. Res.*, *100*, 5599–5612.

Wolf, R. A., V. Kumar, F. R. Toffoletto, G. M. Erickson, A. M. Savoie, C. X. Chen, and C. L. Lemon (2006), Estimating local plasma sheet $PV^{5/3}$ from single spacecraft observations, *J. Geophys. Res.*, *111*, A12218, doi:10.1029/2006JA012010.

Yoon, P. H., and A. T. Y. Lui (2006), Quasilinear theory of anomalous resistivity, *J. Geophys. Res.*, *111*, A02203, doi:10.1029/2005JA011482.

Zhou, M., M. Ashour-Abdalla, X. Deng, D. Schriver, M. El-Alaoui, and Y. Pang (2009), THEMIS observation of multiple dipolarization fronts and associated wave characteristics in the near-Earth magnetotail, *Geophys. Res. Lett.*, *36*, L20107, doi:10.1029/2009GL040663.

Zhou, X.-Z., V. Angelopoulos, V. A. Sergeev, and A. Runov (2010), Accelerated ions ahead of earthward propagating dipolarization fronts, *J. Geophys. Res.*, *115*, A00103, doi:10.1029/2010JA015481.

Zhou, X.-Z., Y. S. Ge, V. Angelopoulos, A. Runov, J. Liang, X. Xing, J. Raeder, and Q.-G. Zong (2012), Dipolarization fronts and associated auroral activities: 2. Acceleration of ions and their subsequent behavior, *J. Geophys. Res.*, *117*, A10227, doi:10.1029/2012JA017677.